Characteristics of a Vertical Metal-Insulator-Metal Microring Cavity

Tae-Young Jeong, Ja-Hyun Gu, Won-Yeol Choi and You-Shin No*

Department of Physics, Konkuk University, Seoul 05029, Korea

We propose a vertical metal-insulator-metal (MIM) plasmonic cavity that comprises top Ag and bottom InGaAsP microring structures on an Ag substrate. A full vectorial numerical simulation was used to characterize the fundamental optical properties of the transverse-magnetic-like plasmonic whispering-gallery-modes (WGMs) excited in a variety of MIM plasmonic cavities. In addition, we exploit the controllability of far-field radiations using the single MIM microring cavity and successfully demonstrate strong directional and localized vertical radiations from the plasmonic WGMs by introducing a number of nanoscale disks along the circumference of the cavity. Our plasmonic cavity can be applied as a component of nanoscale photonic integrated circuits as well as spatially localized out-of-plane optical sensors.

I. INTRODUCTION

Ultrasmall optical cavities are an essential element in a highly integrated photonic circuit [1–3]. They enable efficient photon confinement in small physical volumes [4–9] and serve as coherent light sources with extremely low power consumption [10,11] and fast modulation speed [12]. In particular, plasmonic cavities that integrate additional metal nanostructures with dielectric cavities present a great potential to confine light in a diffraction-limited volume and support resonant modes at deep-subwavelength regime by allowing the excitation of surface-plasmon-polaritons (SPPs) [13–16]. In the previous decade, various plasmonic light sources with enhanced spontaneous emission and subsequent ultralow-threshold lasing operations have been widely reported; for example, electrically-pumped metallic-coated nanocavities that consist of semiconductor heterostructures encapsulated within novel metals showed low-threshold lasing action at a cryogenic temperature [11]. Furthermore, nanodisk/nanopan structures allowed fully three-dimensional (3D) sub-diffraction-limited confinement of mode, thus enabling SPP lasing [5,6,9,11,17]. However, these plasmonic cavities are limitedly applicable to achieve both an efficient light extraction outside the plasmonic cavity and low-loss optical coupling to other photonic elements. Therefore, novel plasmonic cavity structures are still required for practical applications not only for in-plane circuit elements, but also

for out-of-plane device platforms [18,19]. In this study, we propose a plasmonic microring cavity that enables full 3D confinement of the plasmonic mode in an ultra-thin dielectric slab and enhances out-of-plane radiations with controlled directionality. Our numerical simulations show that the proposed cavity supports various plasmonic modes with moderate quality factor of ~ 200 and mode volume of 0.5 $(\lambda/n)^3$; in addition, it demonstrates highly concentrated emission of radiations in a vertical direction with a maximum power enhancement of ~ 800.

II. RESULTS AND DISCUSSION

Figure 1(a) schematically illustrates a plasmonic structure that consists of a metal-semiconductor microring cavity on top of the metal substrate, which forms a vertical metal-insulator-metal (MIM) structure. The metal-semiconductor microring supports various transverse-electric like (TE-like) and transverse-magnetic-like (TM-like) plasmonic whispering-gallery-modes (WGMs) at the interface. In particular, the metal substrate serves as a backside reflector, preventing the extension of the fields of excited plasmonic modes, enabling full 3D confinement of surface plasmons in a subwavelength volume. Figures 1(b) and (c) show the top and side views of the MIM plasmonic cavity with detailed structural parameters as follows; D: diameter of the top Ag and InGaAsP microring, W: width of the microring, h: height of top Ag microring, and $t_{InGaAsP}$: thickness of InGaAsP slab. We performed a 3D finite-difference time-domain (FDTD)
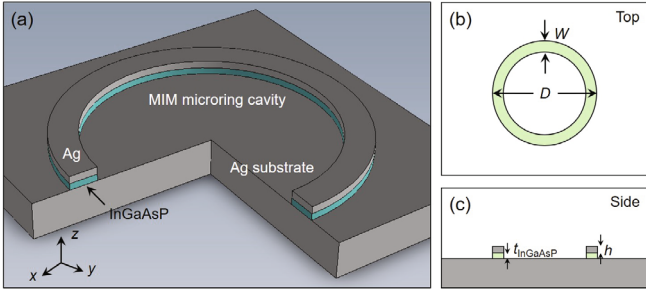
*E-mail: ysno@konkuk.ac.kr; Fax: +82-2-3436-5382

Fig. 1. (Color online) (a) Schematic of the proposed plasmonic microring cavity structure. The InGaAsP microring (cyan) is sandwiched between the Ag microring and substrate (dark gray). (b) and (c) Schematics showing the top (b) and side views (c) of the cavity along with structural parameters; W: width, D: diameter, h: height of the top Ag microring, and t_{InGaAsP}: thickness of InGaAsP slab.

Fig. 2. (Color online) (a) Resonant wavelengths of the excited plasmonic WGMs as a function of microring diameter ranging from 1 to 3 μm. The red circles, blue triangles, and green squares with dotted guidelines of the same color represent the same symmetry groups. (b) - (d) Representative top and side views of the electric field (E_z) profiles of the plasmonic WGMs with different symmetries. The field profiles are obtained from the microring cavities with diameters of 2.3 μm (wavelength: 1583 nm, red-dotted circle), 2.4 μm (wavelength: 1560 nm, blue-dotted circle), and 2.6 μm (wavelength: 1524 nm, green-dotted circle). The modal indices (n, m) are $(1, 15)$, $(1, 16)$, and $(1, 18)$ for diameters of 2.3 μm, 2.4 μm and 2.6 μm, respectively, where n and m are radial and azimuthal mode numbers. The scale bar is 1.0 μm.

simulation to investigate various plasmonic WGMs excited in the cavity; the results of this simulation are shown in Fig. 2. In our simulation, we employed InGaAsP as a high-index semiconductor with an active gain medium wherein the central emission wavelength is near 1.55 μm while using Ag is used as the plasmonic metal. The refractive index of the InGaAsP microring was set to 3.4, and the Ag was described based on the Drude model, which fits the experimentally determined dielectric function. To excite various WGMs, E_z dipole sources with appropriate phases were introduced at the positions where the field intensity maximum was located within the InGaAsP microring cavities. The spatial resolution and domain size in the simulation were 5 nm and $6.0 \times 6.0 \times 0.4 \ \mu\mathrm{m}^3$, respectively. Furthermore, at the boundaries of the simulation domain, we applied perfectly matched layers. In our cavity design, the width and height of the top Ag microring were 200 and 100 nm, respectively. The thin InGaAsP slab with a subwavelength thickness of 90 nm was introduced to only allow plasmonic WGMs. As can be seen in Fig. 2(a), we gradually increased the diameter of the microring cavity from 1 to 3 μm and systematically excited a variety of TM-like plasmonic WGMs where the resonant wavelength range is 1.2 - 1.8 μm. As expected, we observed that the number of plasmonic modes excited in the cavity increased as the diameter of the microring cavity increased. Then, these plasmonic modes were categorized into three different groups based on the symmetry of field distribution. In Fig. 2(a), the circles, triangles, and squares with the same color as well as the dotted guidelines represent the same symmetry groups. Considering the emission bandwidth of the InGaAsP semiconductor, we focus on the excited plasmonic WGMs in the wavelength range of 1.5 - 1.6 μm, which includes the telecommunication C-band (denoted as light green box in Fig. 2(a)). To compare the symmetry of modes, we select three different electric field distributions, as shown in Figs. 2(b) - (d), obtained from the plasmonic microring cavities with diameters of
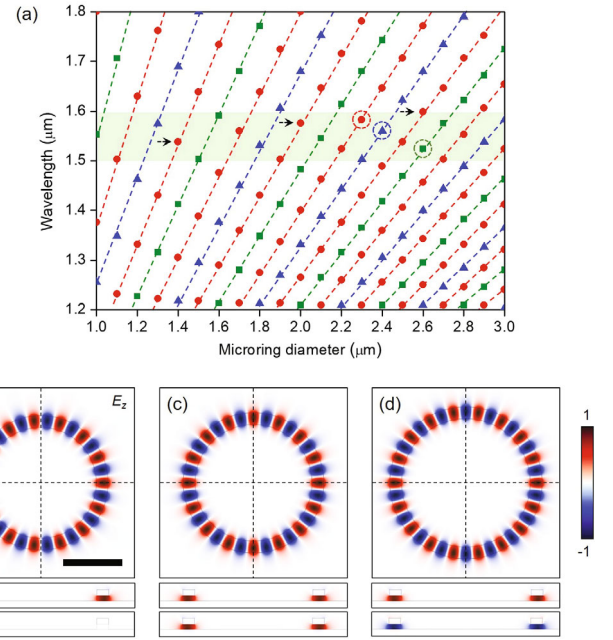
2.3 μm (red dot at 1583 nm in (a)), 2.4 μm (blue triangle at 1560 nm in (a)), and 2.6 μm (green square at 1524 nm in (a)), respectively. They clearly exhibited different symmetry nature of the excited modes. For example, the plasmonic WGM in Fig. 2(b) shows the field intensity maximum and minimum in the microring at x-axis and y-axis, respectively, revealing even and odd symmetries along the respective axes. However, the field distributions shown in Figs. 2(c) and (d) exhibited even symmetry for both x- and y-axes. In addition, the mode in Fig. 2(c) shows the same phase in the field at both x- and y-axes, whereas the mode in Fig. 2(d) shows an opposite phase in field. Furthermore, we observed that the electric fields were tightly confined inside the subwavelength InGaAsP slab sandwiched between the top and bottom metal layers, which successfully satisfies our design goal for fully 3D subwavelength confinement.

To quantitatively investigate the optical properties of plasmonic WGMs, we calculated resonant wavelengths and quality factors for the WGMs excited in a variety of different microring cavities. In Figs. 3(a) and (b), we
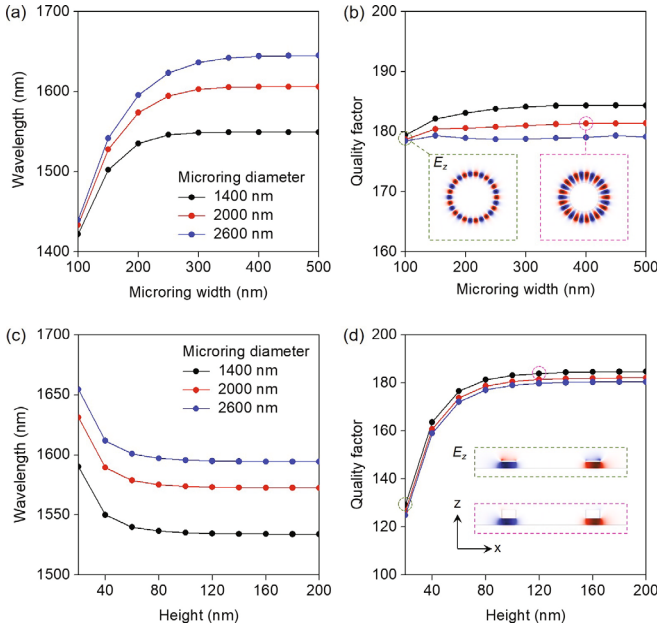
Fig. 3. (Color online) Optical properties of the plasmonic WGMs. (a) and (b) Resonant wavelengths (a) and quality factors (b) with varying microring width for fixed diameters of 1.4 µm (black), 2.0 µm (red), and 2.6 µm (blue). The modal indices are $(1, 9)$, $(1, 13)$ and $(1, 17)$ for diameters of 1.4 µm, 2.0 µm, and 2.6 µm, respectively. These modes are indicated with black arrows in Fig. 2(a). The height of the top Ag microring was set to 100 nm. The insets in (b) are E_z-field profiles for microring widths of 100 nm (left) and 400 nm (right), respectively. (c) and (d) Resonant wavelengths (c) and quality factors (d) with varying height of the top Ag microring for fixed diameters of 1.4 µm (black), 2.0 µm (red), and 2.6 µm (blue). The width of top Ag microring was set to 200 nm. The insets in (d) are side views of the E_z-field profiles for microring heights of 20 nm (left) and 120 nm (right), respectively. For all simulations, the thickness of InGaAsP slab was fixed at 90 nm.

systematically changed the width of the microring cavity for fixed diameters of 1.4, 2.0, and 2.6 µm. The height of the top Ag microring and thickness of the InGaAsP slab were set to 100 and 90 nm for all simulations, respectively. We excited the plasmonic WGMs with field distributions and symmetries similar to the case in Fig. 2(b) and calculated the resonant wavelengths and quality factors as the width of the cavity was varied. We observed that the resonant wavelength of the excited plasmonic WGMs was sensitive to the change in width when the width was smaller than 200 nm for all diameters. For example, the resonant wavelengths were red-shifted by 80 nm (microring diameter: 1.4 µm), 94 nm (microring diameter: 2.0 µm), and 102 nm (microring diameter: 2.6 µm) as the width was increased from 100 to 150 nm. However, the resonant wavelengths changed less rapidly as the width increased beyond 200 nm, and almost remained constant for widths larger than 300 nm. Unlike resonant wavelengths, the quality factors of the plas-

monic WGMs were less sensitive to the change in width, which is shown in Fig. 3(b). As the width increased from 100 to 500 nm, the quality factor for a given diameter remained almost unchanged. These results directly reveal that the plasmonic WGMs can be successfully excited in the subwavelength-scale dimension and can spatially accommodate themselves based on the variations of the cavity structure without noticeable degradation in the quality factor (insets: WGMs of left ($W = 100$ nm) and right ($W = 400$ nm), Fig. 2(b)). In addition, we investigated resonance behavior of plasmonic WGMs while changing height of the top Ag microring; these trends are shown in Figs. 3(c) and (d). In our study, we fixed the width of both the top Ag and InGaAsP microrings to 200 nm; further, the 90-nm-thick InGaAsP slab was unchanged. The results in Fig. 3(c) shows that the resonant wavelengths were significantly blue-shifted with a small increase in height when the height was less than 60 nm. For example, when the height was changed from 20 nm to 40 nm, the observed wavelength shifts were 40 nm (microring diameter: 1.4 µm), 42 nm (microring diameter: 2.0 µm), and 43 nm (microring diameter: 2.6 µm). However, for heights greater than 80 nm, a major shift in resonant wavelength was not observed. These observations can be attributed to the ultrathin top metal microring structure that allows plasmonic WGMs to experience not only the bottom, but also the side and top surfaces of the metal structure. Consequently, it leads to the increase in the effective modal area and subsequently the resonant wavelength. The calculated quality factors in Fig. 3(d) support this explanation. There is a significant decrease in the quality factor of the plasmonic WGMs excited in the cavity structures with small heights ($h < 60$ nm), which can be attributed to the abovementioned increase in effective area of the plasmonic mode and corresponding metallic loss. The spatial distributions of the electric fields of plasmonic WGMs for small (20 nm) and large (120 nm) heights (top and bottom insets, Fig. 3) further confirmed our analysis. For sufficiently large heights (> 80 nm), the quality factors of plasmonic WGMs remained unchanged for all diameters. We note that similar spectral behaviors and variations of quality factor were observed in other plasmonic WGMs with different symmetries.

Furthermore, we investigated the controllable optical properties of the excited plasmonic WGMs for various key applications. In particular, we focused on directional far-field emission from our plasmonic microring cavity. Since the excitation of SPPs occurs at the interface between the metal and dielectric material, it is not straightforward to control the directionality of far-field emission of the plasmonic modes. In addition, the transversely traveling nature of WGMs within the microdisk or microring cavities makes it difficult to observe a strong far-field emission pattern in the vertical direction [3,6,9]. For example, we calculated the z-component of the time-averaged Poynting vectors from a single MIM microring cavity structure in Fig. 4(a). Here, the di-
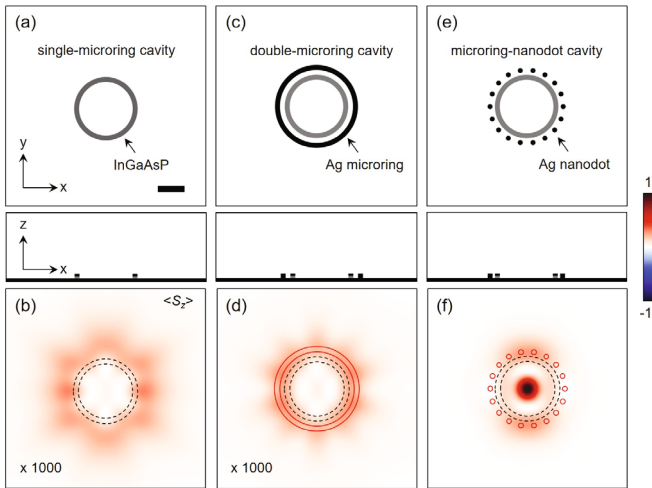
Fig. 4. (Color online) Vertical emissions of radiations from various plasmonic cavities. Simulation structures of a vertical MIM single-microring cavity (a), double-microring cavity (c), and microring-nanodot cavity (e). (a) Diameter of single-microring was 2.6 μm and the width and height of the top Ag microring were set to 200 nm and 100 nm, respectively. The resonant mode used in (a) has a modal index of $(1, 17)$. The scale bar in (a) is 1.0 μm. (c) Diameter of the additional Ag microring (black ring) was 3.4 μm and the width and height were set to 200 nm and 190 nm, respectively. (e) Eighteen nanodots (black circles) were introduced to the single-microring cavity. The diameter of a single nanodot was 200 nm, while the gap between the nanodots and inner microring was 100 nm. Calculated z-component of the time-averaged Poynting vectors obtained from the single-microring (b), double-microring (d), and microring-nanodot cavities (f), respectively. For visual comparison, the intensity of the Poynting vectors in (b) and (d) were increased 1000-fold. An identical color bar was used to describe the Poynting vectors in (b), (d), and (f).

ameter of the microring was 2.6 μm, while the width and height of the top metal microring were 200 nm and 100 nm, respectively. The thickness of the InGaAsP slab was 90 nm, and the Poynting vectors were recorded at a position 1 μm above the top metal layer. As shown in Fig. 4(b), a considerably weak and delocalized vertical emission of the electromagnetic fields was observed from the plasmonic WGM, which restricts the application of our plasmonic cavity to in-plane device platforms. To address this limitation and improve the vertical extraction of radiations, we introduced two types of light extraction structures and examined their feasibility. First, an additional concentric Ag microring with a diameter of 3.4 μm was introduced to the single plasmonic cavity, which formed a double-microring cavity as shown in Fig. 4(c). In this case, the additionally introduced Ag microring was not physically in contact with the InGaAsP active medium; therefore, significant metallic loss and serious field deformations were not expected. Furthermore, the width and height were the same as those of the single plasmonic cavity shown in Fig. 4(a). The

calculated z-component of the time-averaged Poynting vectors in Fig. 4(d), however, showed only a slight difference in the spatial emission pattern compared with that of the single cavity. The vertical emission of electromagnetic radiations was still negligible. Next, we employed the concept of optical gratings and introduced multiple nanoscale Ag disks, termed nanodots, around the single plasmonic cavity and these adjacent nanodots were equally spaced in a circular fashion; this is shown in Fig. 4(e). It is well-known that the linear metallic and dielectric grating structures enable an efficient in-coupling (out-coupling) between in-plane optical devices and vertically in-coming (out-going) radiations [18,19]. In addition, controlling the grating parameters (*i.e.*, pitch, depth, and width) determines how efficiently one can achieve the radiation coupling. To capitalize on this concept, in our study, we designed the circular metallic gratings consisting of multiple nanodots, which enabled the circularly traveling surface plasmons in the cavity to effectively experience an infinite grating [19]. In addition, we also introduced a small space (the gap: g) between the inner microring and nanodots to prevent unwanted metallic loss and major perturbation or distortion of the plasmonic WGMs. There were various configuration parameters such as the number of nanodots, gap between microring and nanodots, as well as diameter and height of a single nanodot. In Fig. 4(e), we initially designed eighteen single nanodots with a diameter and height of 200 nm and 190 nm, respectively. The gap size was set to 100 nm. This nanodot grating structure led to an unexpected successful result; in particular, as shown in Fig. 4(f), we can clearly observe that not only was there considerable enhancement in the vertical emission, but also a strongly concentrated far-field radiation pattern at the center. For direct, visual comparison, we used an identical intensity color bar and normalized the time-averaged Poynting vectors in Fig. 4; the Poynting vectors from single- and double-microring cavities were increased 1000-fold in intensity to make them visually discernible. The observed directional and enhanced vertical emission can be understood as a consequence of the interaction between the plasmonic WGM and array of the periodically spaced nanodots. Without nanodot gratings, the electric fields of the plasmonic WGMs in single- and double-microring cavities were tightly confined inside the InGaAsP slab and no fields outside the slab propagated towards the center or out of the microring. However, the introduction of individual nanodots perturbed the fields of plasmonic WGM and provided additional wavevectors that could escape from the InGaAsP slab and propagate towards the center of the microring. The far-field radiation of these wavevectors constructively interfere and lead to an enhanced and strongly localized vertical emission. In addition, we note that the spatial distribution of far-field emission can be controlled by changing the configuration parameters and manipulating the near-field interaction.

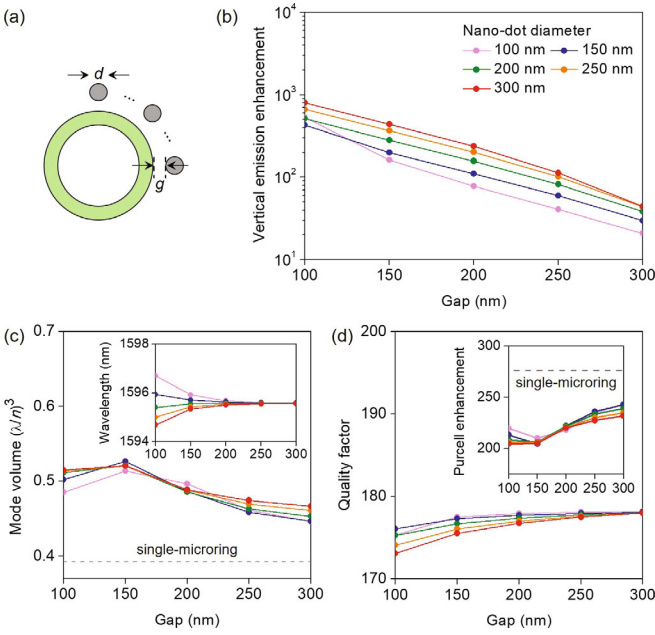In order to quantitatively investigate vertical emission

Fig. 5. (Color online) (a) Schematic showing structural parameters of microring-nanodot cavities; d: diameter of a single nanodot, g: gap size between nanodots and microring. (b) Vertical emission enhancements versus gap size and diameter of a single nanodot. The enhancements were calculated by integrating the vertical component of the Poynting vectors from the microring-nanodot cavities and normalizing them with that of a single-microring cavity. Single nanodots with diameters of 100 nm (pink), 150 nm (navy), 200 nm (cyan), 250 nm (yellow), and 300 nm (red) were simulated. (c) - (d) Mode volumes (c) and quality factors (d) of the plasmonic WGMs excited in the microring-nanodot cavities. Insets of (c) and (d) show the calculated resonant wavelengths and Purcell enhancement factors.

of radiations from plasmonic WGMs, we simulated various microring-nanodot cavities. For a fixed microring cavity, we systematically varied the gap between the microring and nanodots from 100 nm to 300 nm for five different diameters of 100, 150, 200, 250, and 300 nm, respectively (Fig. 5(a)). Here, the microring of Fig. 4(a) was used for all simulations. Furthermore, as shown in Fig. 5(b), we calculated vertically emitting electromagnetic radiation powers by integrating the time-averaged Poynting vectors passing through the detection plane of 10×10 μm^2 positioned 1 μm above the cavities. Then, we normalized the powers using that of the single MIM microring cavity to obtain vertical emission enhancement and plotted them as a function of the gap and diameter. Notably, we observed that the maximum vertical emission enhancement was ~ 800 for a gap size of 100 nm and nanodot diameter of 300 nm. In addition, we observed the vertical radiation power decreased as the gap size increased; in particular, the enhancement significantly decreased from 535 to 162 when the gap size was increased from 100 to 150 nm. As the size of nanodots increased with a fixed gap size, the enhance-

ment increased as well. These results unambiguously support our previous analyses shown in Fig. 4. The vertical directional radiations originate from the near-field interaction of circularly traveling plasmonic WGMs with effectively infinite, circular gratings. Furthermore, we investigated the changes in the fundamental optical properties of the excited mode as the gap and diameter was varied. Figures 5(c) and (d) show the calculated mode volumes and quality factors of the plasmonic WGMs supported in various microring-nanodot cavities. As expected, the introduced nanodots resulted in a slight increase in mode volume for small gap sizes due to the considerable near-field interaction and corresponding delocalization of fields. Subsequently, the resonant wavelengths shifted as well. However, the variations for all cavity structures considered in our study were not significant compared with the mode volume of the single MIM microring cavity. In addition, the calculated quality factors also showed a minor change for small gap sizes, which was less by an order compared with that of the single cavity. Finally, we calculated the Purcell enhancement factors and compared them with that for the single MIM microring cavity (Purcell factor: ~ 280) to evaluate the effect of nanodots on the quality of the cavity (inset, Fig. 5(d)); the plot shows an overall decrease in Purcell factors, which was inevitable because of the increased modal volumes and decreased quality factors. However, the Purcell factors still remained over 200 for even the smallest gap size of 100 nm considered in our study, exhibiting high quality as a microcavity. In summary, the results in Fig. 5 reveal that controlled introduction of nanodots can significantly enhance the vertical emission power, while preserving the fundamental optical qualities of the cavity.

III. CONCLUSION

In conclusion, we designed a vertical MIM plasmonic cavity consisting of an Ag top and 90-nm-thick bottom of InGaAsP microrings on an Ag substrate. A full 3D FDTD simulation was performed to simulate various cavity structures with different diameters, widths, and heights of the top and bottom microrings. We systematically categorized the excited TM-like plasmonic WGMs based on the symmetry of fields and intensity distributions; in addition, we investigated the fundamental optical properties of the different modes. Furthermore, resonant behaviors because of structural variations of the cavity were analyzed. In addition, we designed multiple nanodots along the circumference of the single MIM microring cavity and demonstrated a significant enhancement of far-field radiations as well as a strongly directional emission pattern without major degradation of optical properties of modes as a consequence of the nanodots. We believe that this plasmonic cavity can be useful in ultracompact integrated photonic circuits as well as

in out-of-plane device platforms, such as terahertz light sources and biochemical sensors and detectors.

ACKNOWLEDGMENTS

REFERENCES

[1] L. Liu *et al.*, Nat. Photonics **4**, 182 (2010).
[2] M. T. Hill *et al.*, Nature **432**, 206 (2004).
[3] H-G. Park, C. J. Barrelet, Y. Wu, B. Tian, F. Qian and C. M. Lieber, Nat. Photonics **2**, 622 (2008).
[4] J-H. Kang, H-G. Park and S-H. Kwon, Opt. Express **19**, 13892 (2011).
[5] K. Yu, A. Lakhani and C. Wu, Opt. Express **18**, 8790 (2010).
[6] M. P. Nezhad, A. Simic, O. Bondarenko, B. Slutsky, A. Mizrahi, L. Feng, V. Lomakin and Y. Fainman, Nat. Photonics **4**, 395 (2010).
[7] R. F. Oulton, V. J. Sorger, T. Zentgraf, R-M. Ma, C. Gladden, L. Dai, G. Bartal and X. Zhang, Nature **461**, 629 (2009).
[8] R-M. Ma, R. F. Oulton, V. J. Sorger, G. Bartal and X. Zhang, Nat. Mater. **10**, 110 (2011).
[9] S-H. Kwon, J-H. Kim, C. Seassal, S-K. Kim, P. Regreny, Y-H. Lee, C. M. Lieber and H-G. Park, Nano Lett. **10**, 3679 (2010).
[10] H-G. Park, S-H. Kim, S-H. Kwon, Y-G. Ju, J-K. Yang, J-H. Baek, S-B. Kim and Y-H. Lee, Science **305**, 1444 (2004).
[11] M. T. Hill *et al.*, Nat. Photonics **1**, 589 (2007).
[12] D. Englund, H. Altug, B. Ellis and J. Vučković, Laser Photon. Rev. **2**, 264 (2008).
[13] W. L. Barnes, A. Dereux and T. W. Ebbesen, Nature **424**, 824 (2003).
[14] H. T. Miyazaki and Y. Kurokawa, Phys. Rev. Lett. **96**, 097401-1 (2006).
[15] S. A. Maier, *Plasmonics: Fundamentals and Applications* (Springer-Verlag, New York, 2007).
[16] M. L. Brongersma and P. G. Kik, *Surface Plasmon Nanophotonics* (Springer-Verlag, New York, 2007).
[17] S-H. Kwon, J-H. Kang, S-K. Kim and H-G. Park, IEEE J. Quantum Electron. **47**, 1346 (2011).
[18] J-S. Park *et al.*, Nano Lett. **17**, 7731 (2017).
[19] L. Mahler, A. Tredicucci, F. Beltram, C. Walther, J. Faist, B. Witzigmann, H. E. Beere and D. A. Ritchie, Nat. Photonics **3**, 46 (2009).